Primary- and secondary-sphere effects of amine substituent position on rhenium bipyridine electrocatalysts for CO_2 reduction

Ashley N. Hellman, Jeremy A. Intrator, Jeremiah Choate, David A. Velazquez, and Smaranda C. Marinescu*

Abstract: It is well-established that electrocatalysts with biologically inspired moieties provide advantageous qualities for the efficient transformation of fossil fuel combustion products, such as carbon dioxide, into value-added products. Herein, we present a family of $Re(bpy)(CO)_3Cl$ electrocatalysts with pendant NH_2 groups in the 4,4'-, 5,5'-, and 6,6'-positions of the bipyridine backbone with the objective of determining the effects of combined primary- and secondary-sphere interactions on the reduction of CO_2 to CO. Cyclic voltammetry studies under CO_2 indicate that the catalytic onset potential is more positive for 6,6'-NH_2-Re, indicating that proximity of the available pendant protons to the metal center is beneficial during catalysis. Controlled potential electrolysis studies demonstrate that, similar to 6,6'-NH_2-Re, 4,4'-NH_2-Re displays a dependence of Faradaic efficiency (FE) on catalytic potential, reaching a maximum FE_{CO} of 91% at -2.40 V. This FE is greater than that observed for 6,6'-NH_2-Re but occurs at a more negative potential. Density functional theory (DFT) calculations were performed to compare the HOMO-LUMO gap of these complexes, and the following trend of 4,4'-NH_2-Re > 6,6'-NH_2-Re > 5,5'-NH_2-Re was determined. Mulliken electron population analysis indicates a greater degree of electron density on the metal center for 6,6'-NH_2-Re compared to its related congeners, in agreement with the electrolysis studies which illustrate a more favorable CO_2 reduction for 6,6'-NH_2-Re. Ultimately, it is important that the various catalytic parameters are properly balanced to provide the greatest overall catalytic activity.

Keywords: electrochemistry, molecular electrocatalysis, pendant protons, hydrogen bonding, substituent effects

1. Introduction

The effects of climate change are detrimental to both the environment and society. With a significant portion of infrastructure based on the consumption of fossil fuels, it is paramount to develop the technology to convert small molecules into renewable fuel sources.[1] Specifically, the conversion of carbon dioxide (CO_2) into useful products is beneficial in that it allows for recycling of harmful combustion by-products while working toward a carbon-neutral infrastructure.[2] In order to overcome the high thermodynamic barrier associated with the conversion of CO_2 to carbon monoxide (CO), catalysts must be designed and employed.[3] Throughout its evolutionary history, the CO-dehydrogenase (CODH) enzyme in nature has adapted to efficiently and selectively reduce CO_2 to CO.[4–6] In recent years, chemists have aimed to emulate nature by tuning both the electronic effects of the primary coordination sphere, and the through-space effects of the secondary coordination sphere. Specifically, altering the position and electron-withdrawing nature of a functional group on the ligand backbone of the catalyst can influence such catalytic parameters as the overpotential, and adding and properly positioning available pendant proton donors can assist with stabilization of the CO_2 adduct that forms during catalysis, enhancing overall catalytic activity.

A variety of bio-inspired CO_2 reduction electrocatalysts have been designed to date,[7] including (but not limited to) nickel cyclams with pendant amines,[8–10] iron porphyrins with pendant phenolic,[11] trimethylanilinium,[12] and amide groups,[13] and cobalt aminopyridine macrocycles with pendant amines.[14–

[16] Further, many rhenium[17–29] and manganese[30–35] bipyridine catalysts, such as Re(bpy)$(CO)_3$Cl and Mn(bpy)$(CO)_3$Br, where bpy = 2,2′-bipyridine, with pendant proton donors and resulting second-sphere interactions have also been reported.[36] Positional effects of methyl substituents on the bipyridine backbone have been investigated,[37] as well as the electronic effects from altering the electron-donating or -withdrawing nature of substituents within the same position on the ligand.[38–40] These studies, among other examples published in the literature,[41,42] demonstrate that both sterics and electronics influence the electrocatalytic behavior. However, a small number of CO_2 reduction electrocatalysts exist that investigate tandem primary and secondary coordination sphere effects.

We previously studied a family of 6,6'-substituted rhenium bipyridine complexes with primary, secondary, and tertiary amines to determine the effect of available pendant protons on the electrocatalytic activity, wherein the -NH_2 substituted complex (6,6'-NH_2-Re) underwent hydrogen bonding interactions and outperformed 6,6'-NHMe-Re and 6,6'-NMe_2-Re.[43] Building upon these studies, we report here the synthesis, characterization and electrochemistry of a novel 4,4'-NH_2 substituted Re(bpy)$(CO)_3$Cl complex (4,4'-NH_2-Re, Scheme 1), along with more in depth electrochemical studies of the previously reported 5,5'-substituted analogue (5,5'-NH_2-Re).[28] We further sought to more directly compare 4,4'-NH_2-Re with our previously studied 5,5'-NH_2-Re and 6,6'-NH_2-Re to determine the electronic and steric positional effects of the -NH_2 substituent on the electrocatalytic activity for the reduction of CO_2 to CO.

2. Materials and methods

2.1. General methods

All manipulations of air and moisture sensitive materials were conducted under a nitrogen atmosphere in a Vacuum Atmospheres drybox or on a dual manifold Schlenk line. The glassware was oven-dried prior to use. All solvents were degassed with nitrogen and passed through activated alumina columns and stored over 4Å Linde-type molecular sieves. Deuterated solvents were dried over 4Å Linde-type molecular sieves prior to use. Proton NMR spectra were acquired at room temperature using Varian (Mercury 400 2-Channel, VNMRS-500 2-Channel, VNMRS- 600 3-Channel, and 400- MR 2-Channel) spectrometers and referenced to the residual ^{1}H resonances of the deuterated solvent (^{1}H: DMSO-d_6) and are reported as parts per million relative to tetramethylsilane. Elemental analyses were performed using Thermo Scientific™ FLASH 2000 CHNS/O Analyzers. All the chemical reagents were purchased from commercial vendors and used without further purification.

2.2. Electrochemistry

Electrochemistry experiments were carried out using a Pine potentiostat. The experiments were performed in a single compartment electrochemical cell under nitrogen or CO_2 atmosphere using a 3 mm diameter glassy carbon electrode as the working electrode, a platinum wire as the auxiliary electrode and a silver wire as the reference electrode. Ohmic drop was compensated using the positive feedback compensation implemented in the instrument. All electrochemical experiments were performed with iR compensation using the current interrupt (RUCI) method in AfterMath. Typical values for the cell resistance were around 160-170 ohms. All potentials in this paper were referenced relative to ferrocene (Fc) with the $Fe^{3+/2+}$ couple at 0.0 V. Alternatively, in cases when the redox couple of ferrocene overlapped with other features of interest, decamethylferrocene (Fc*) was used as an internal standard with the $Fe^{*3+/2+}$ couple at –0.48 V. All electrochemical experiments were performed with 0.1 M tetrabutylammonium hexafluorophosphate ($TBAPF_6$) as the supporting electrolyte. The concentrations of the rhenium catalysts were generally at 1 mM and experiments with CO_2 were performed at gas saturation in acetonitrile (MeCN) or dimethylformamide (DMF).

Controlled-potential electrolysis (CPE) measurements were conducted in a two-chamber H cell. The first chamber held the working and reference electrodes in 40 mL of 0.1 M $TBAPF_6$ and TFE in MeCN or DMF.

The second chamber held the auxiliary electrode in 25 mL of 0.1 M $TBAPF_6$ in MeCN or DMF. The two chambers were separated by a fine porosity glass frit. The reference electrode was placed in a separate compartment and connected by a Vycor tip. Glassy carbon plate electrodes (6 cm × 1 cm × 0.3 cm; Tokai Carbon USA) were used as the working and auxiliary electrodes. Using a gas-tight syringe, 2 mL of gas were withdrawn from the headspace of the H cell and injected into a gas chromatography instrument (Shimadzu GC-2010-Plus) equipped with a BID detector and a Restek ShinCarbon ST Micropacked column. The method file created is meant to detect all possible gases with the best separation up to a retention time of 15 minutes with a ramp up rate of 8°C/min to a max of 180°C to clear the column of any impurities or residual gases. Faradaic efficiencies were determined by dividing the measured CO produced by the amount of CO calculated based on the charge passed during the CPE experiment. The reported Faradaic efficiencies and μmol of CO produced are average values.

2.3. Computational methods

All calculations were run using the Q-CHEM program package.[44] Level of theory was determined based on previous a computational report on the 5,5'-NH_2Re system.[28] Geometry optimizations were run with restricted DFT calculations at the M06 level of theory with a composite basis set. The Pople 6-31G* basis set was used for H,C,N, and O atoms and the Hay–Wadt VDZ (n + 1) effective core potentials and basis sets (LANL2DZ) were used for Cl and Re atoms.[45–52]All optimized geometries were verified as stable minima with frequency calculations at the same level of theory. The M06 functional was used throughout this study, as it provides reduced Hartree–Fock exchange contributions and includes empirical fitting for accuracy in organometallic systems.[53] Single point energy calculations were run with a larger 6-311G** basis for H, C, N, and O atoms and solvation was treated with COSMO (dielectric constant of 37.5 for acetonitrile).[54] Kohn–Sham orbital images are presented with isovalues of 0.05 for clarity.

2.4. Synthesis

[Re(4,4'-NH_2-bpy)$(CO)_3$Cl] (4,4'-NH_2-Re). Under N_2, [2,2'-bipyridine]-4,4'-diamine (4,4'-NH_2-L, >98% purity, 102 mg, 0.55 mmol) and $Re(CO)_5Cl$ (98% purity, 199 mg, 0.55 mmol) were refluxed in 30 mL anhydrous toluene for 18 hours. After cooling, the resulting precipitate was collected by vacuum filtration and washed with ether, yielding a yellow solid in approximately 94% yield. ^{1}H NMR (DMSO-d_6): δ 8.22 (d, 1H, NC_5H_3), 7.21 (s, 1H, NC_5H_3), 7.12 (s, 2H, NH_2), 6.65 (d, 1H, NC_5H_3) ppm. Anal. Calcd. for $C_{13}H_{10}ClN_4O_3Re$: C, 31.74; H, 2.05; N, 11.39. Found: C, 30.10; H, 1.78; N, 10.31.

2.5. X-ray Crystallography

A clear green needle specimen was mounted for the X-ray crystallographic analysis, with approximate dimensions of 0.118 × 0.108 × 0.028 mm^3. The X-ray intensity data were measured on a XtaLAB Synergy, Dualflex, HyPix system equipped with a micro-focus sealed tube (Cu Kα λ = 1.54184 Å), a goniometer (4-axis kappa with telescopic detector sled), and a detector (HPC HyPx-6000HE 77.5 × 80.3 mm^2). Data was collected on CrysAlisPro 1.171.41.122a (Rigaku OD, 2021) and a total of 2566 frames were collected and integrated. The SHELXT 2014/5 Software Package was used to determine the structure solution with direct methods. The SHELXL Software Package was used for refinement by full-matric least-squares on F2. OLEX2-1.5 program was used for both structure solution and refinement.

2.6. Physical Methods

X-ray Photoelectron Spectroscopy (XPS) data were collected using a Kratos AXIS Ultra instrument. The monochromatic X-ray source was the Al K α line at 1486.6 eV. High-resolution detailed scans, with a resolution of ~0.1 eV, were collected on individual XPS lines of interest at a pass energy of 20. The sample chamber was maintained at < 2 × 10^{-8} Torr. The XPS data were analyzed using the CasaXPS software.

High-resolution scanning electron microscopy (HR-SEM) was performed on a FEI Nova NanoSEM 450 scanning electron microscope using an accelerating voltage of 15 kV.
UV-Vis spectra were collected using an Agilent Technologies Cary 60 UV-Vis spectrophotometer. Samples of the rhenium complexes in acetonitrile were studied in transmittance mode and the spectrum of acetonitrile was subtracted as background.
FT-IR spectra were acquired using a Bruker Vertex 80v spectrometer. Samples (2 mg) for analysis were mixed into a KBr (100 mg) matrix and pressed into pellets.

3. Results and Discussion

3.1. Synthesis and Characterization

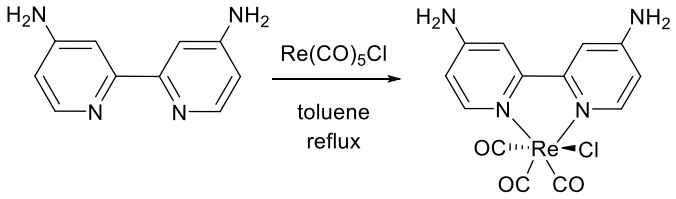

Scheme 1. Synthesis of complex 4,4'-NH_2-Re.

Synthesis of ligand 4,4'-NH_2-L was adapted from literature procedures.[55,56] Upon isolation of the ligand, complex 4,4'-NH_2-Re was synthesized via reflux of 4,4'-NH_2-L and $Re(CO)_5Cl$ in anhydrous toluene overnight (Scheme 1). Following collection of the precipitate, ^1H nuclear magnetic resonance (NMR) of 4,4'-NH_2-Re in DMSO-d_6 displays three aromatic peaks: a doublet at δ 8.22 ppm, a singlet at δ 7.21 ppm, and another doublet at δ 6.65 ppm in a 1:1:1 ratio, assigned to the protons along the backbone of the bipyridine ring (Figure S1). An additional 2*H* singlet at δ 7.12 ppm is assigned to the symmetric NH_2 substituents in the 4- and 4'-positions of the bipyridine ring. The small singlet at δ 7.95 ppm represents the protons of co-crystallized *N,N*-dimethylformamide (DMF). The complex 4,4'-NH_2-Re was further characterized by UV-vis, displaying a characteristic $Re(bpy)(CO)_3Cl$ peak at 350 nm (Figure S2), and by elemental analysis (EA).

Yellow crystals of 4,4'-NH_2-Re were grown from vapor diffusion of ether into a DMF solution of the complex (Figure S17). Single crystal X-ray diffraction studies display a six coordinate Re(I) metal center and facial arrangement of three carbonyl moieties, analogous to typical $Re(bpy)(CO)_3$ complexes (Figure 1).[47] The bipyridine ligand occupies a quasi-equatorial coordination and is significantly more planar than 6,6'-NH_2-Re due to less steric hindrance around the Re center. The Re–N(bpy) bond lengths (2.174(4) Å and 2.165(3) Å) in 4,4'-NH_2-Re are shorter than those of 6,6'-NH_2-Re (2.178(2) Å and 2.190(2) Å), consistent with less steric bulk and greater planarity. A notable feature of the crystal structure of 4,4'-NH_2-Re is that the co-crystallized DMF is oriented with the oxygen atom of DMF pointing directly to the nitrogen atom of the pendant amine. A similar behavior was observed for the 6,6'-NH_2-Re analogue.[43] The distance between the O and N atoms in 4,4'-NH_2-Re is 2.884 Å, which is slightly longer than the one observed for 6,6'-NH_2-Re, although still within the bond length of a hydrogen bond (Figure 1a). This interaction again illustrates the affinity of these NH_2-substituted complexes for forming hydrogen bonds even in the solid state.

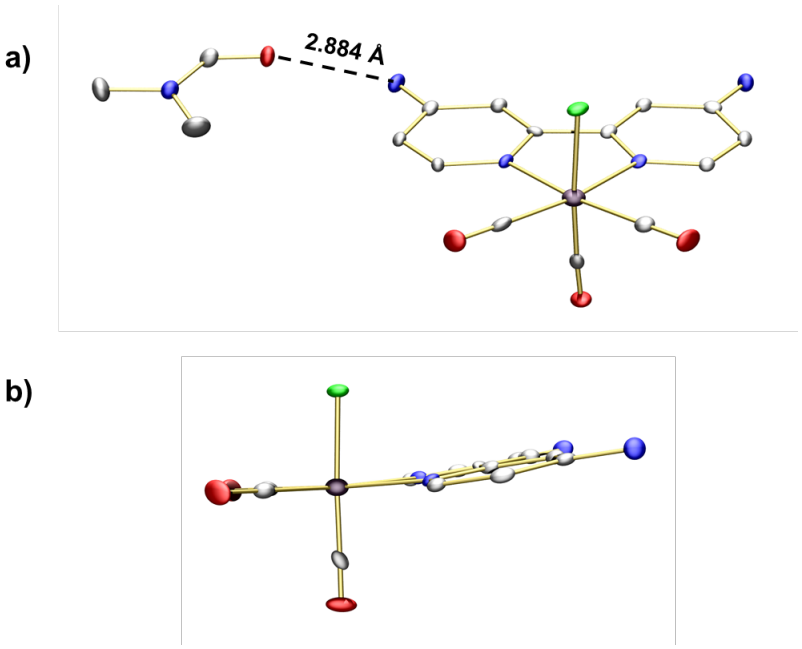

Figure 1. Solid state structure of 4,4'-NH_2-Re, (a) front view including hydrogen bond distance between the pendant amine and co-crystallized DMF and (b) side view. Color legend of the atoms: gray – C; blue – N; red – O; green – Cl; purple – Re. Hydrogen atoms are excluded for clarity.

Complex 4,4'-NH_2-Re was further characterized by FT-IR spectroscopy (Figure S3). Three carbonyl stretches are observed at 2014, 1917, and 1869 cm^{-1}, corresponding to one high-energy mode (a_1') and two lower-energy modes (a" and a_2'), as expected for *fac*-$Re(CO)_3$ complexes and similar to those observed for 6,6'-NH_2-Re. There are also several primary amine asymmetric and symmetric N-H stretches at 3493, 3405, 3308, and 3200 cm^{-1}, as well as a strong -NH_2 scissoring absorption at 1640 cm^{-1}. The sharper -NH_2 stretches compared to the broad ones observed for 6,6'-NH_2-Re suggest that hydrogen bonding interactions are less favorable for this complex.[59,60]

3.2. Cyclic Voltammetry

For comparison of the electrochemical behavior of 4,4'-NH_2-Re to our previously reported 5,5'-NH_2-Re and 6,6'-NH_2-Re, cyclic voltammetry (CV) studies were first performed under N_2 in acetonitrile (MeCN) solutions (1 mM catalyst with 0.1 M tetrabutylammonium hexafluorophosphate [$TBAPF_6$] as the supporting electrolyte). All electrochemical potentials discussed are referenced versus $Fc^{+/0}$. CVs of 4,4'-NH_2-Re display an irreversible reduction event at -2.14 V, followed by a second broad and weak irreversible reduction event near -2.46 V, both of which do not gain reversibility with faster scan rates (Figure 2, Table 1). The Randles-Sevcik analysis performed on the first reduction feature reveals a slope of 0.5, indicating that this complex is freely diffusing in solution (Figure S4). This electrochemical behavior is analogous to that observed for 5,5'-NH_2-Re, which displays irreversible reduction features at -2.11 and -2.47 V.[28] The electrochemical behavior of both 4,4'-NH_2-Re and 5,5'-NH_2-Re, however, differs from that of 6,6'-NH_2-Re, which displays three irreversible reduction events under N_2 at -2.00 V, -2.11 V, and -2.23 V.[39] The more negative reduction potentials of 4,4'-NH_2-Re and 5,5'-NH_2-Re, compared to those of 6,6'-NH_2-Re, suggests that these complexes are more difficult to reduce, potentially due to the positions of the NH_2 substituents on the bipyridine backbone. Further, the lack of the additional intermediate feature observed in the CVs of 6,6'-NH_2-Re, which was attributed to intermolecular hydrogen bonding interactions, is not apparent in the

CVs of 4,4'-NH_2-Re and 5,5'-NH_2-Re, suggesting that the position of the NH_2 groups on the bipyridine backbone influences the hydrogen bonding capabilities of the amine-substituted Re(bpy) complexes.

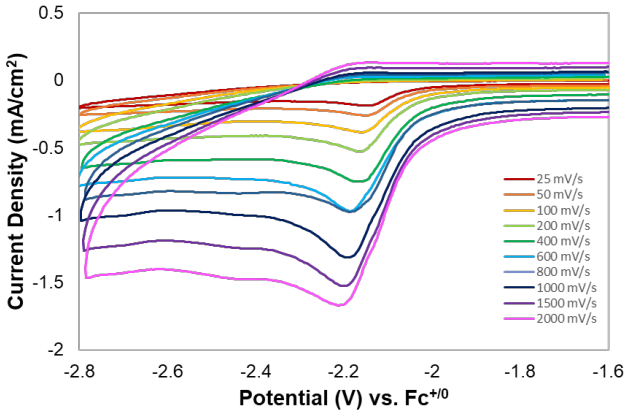

Figure 2. Variable scan rate CVs of 4,4'-NH_2-Re under N_2. Conditions: 1 mM catalyst in MeCN with 0.1 M $TBAPF_6$; scan rate: 100 mV/s.

Table 1. Reduction potentials (V vs. $Fc^{+/0}$) for 4,4'-NH_2-Re, 5,5'-NH_2-Re, and 6,6'-NH_2-Re in MeCN and DMF under N_2. Scan rate: 100 mV/s.

Catalyst	**1st reduction**		**Intermediate reduction**		**2nd reduction**	
	MeCN	DMF	MeCN	DMF	MeCN	DMF
4,4'-NH_2-Re	-2.14	-2.17	--	--	-2.46	-2.44
5,5'-NH_2-Re[28]	-2.11	-2.21	--	--	-2.47	--
6,6'-NH_2-Re[43]	-2.00	-2.06	-2.11	--	-2.23	-2.42

Further electrochemical studies of 4,4'-NH_2-Re and 5,5'-NH_2-Re were performed in DMF to investigate how the position of the NH_2 substituent influences intermolecular hydrogen bonding interactions in these complexes. Since DMF is a significantly better hydrogen bond donor and acceptor than MeCN, it can disrupt intermolecular hydrogen bonding interactions, leading to an observable change in the electrochemical behavior. CVs of 4,4'-NH_2-Re and 5,5'-NH_2-Re in DMF display only moderately different behavior than that observed in MeCN, compared to 6,6'-NH_2-Re, which differs more significantly upon change in solvent (Figure 3, Table 1). Under N_2, 4,4'-NH_2-Re exhibits an irreversible reduction event at -2.17 V, followed by a second broad and weak irreversible reduction event at -2.44 V, analogous to the features observed in MeCN. Similarly, 5,5'-NH_2-Re exhibits a quasi-reversible reduction event at -2.21 V, slightly more negative than the corresponding feature in MeCN. However, the lack of a second reduction event and the appearance of a small oxidation feature suggest that the solvent does slightly influence the behavior of 5,5'-NH_2-Re. Upon increasing the scan rate, the behavior of both 4,4'-NH_2-Re and 5,5'-NH_2-Re changes more substantially (Figures S5 and S6). The second reduction feature of 4,4'-NH_2-Re grows in more strongly, and the reduction features of both complexes become more quasi-reversible, suggesting that at faster scan rates, these electrochemical processes can outcompete the irreversible chemical ones that may influence hydrogen bonding. These results indicate that the position of the NH_2 groups on the bipyridine backbone influences the extent to which these amine-substituted complexes can undergo hydrogen bonding interactions, based on the electrochemical differences observed for each of these complexes upon switching from MeCN to DMF.

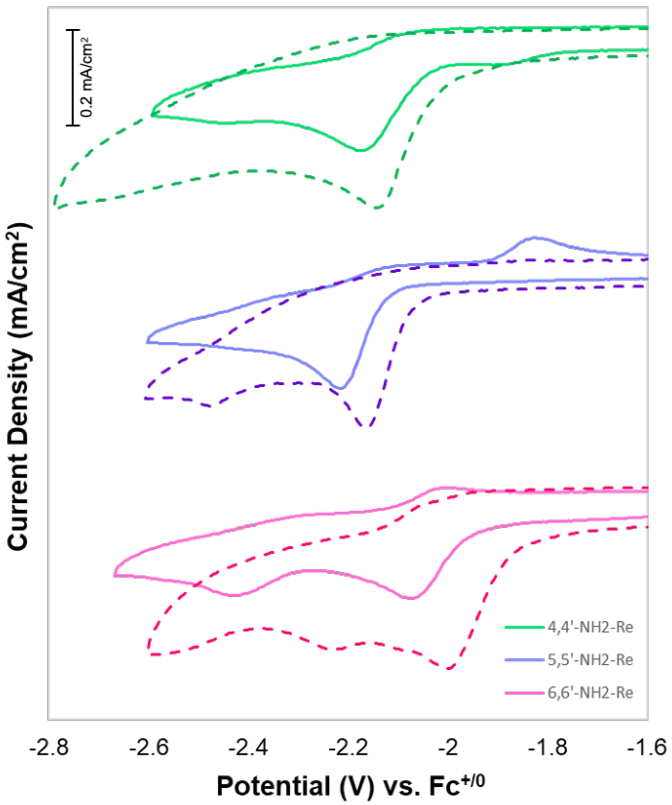

Figure 3. Overlay of cyclic voltammograms of 4,4'-NH_2-Re (green), 5,5'-NH_2-Re (purple), and 6,6'-NH_2-Re (pink) under N_2 in MeCN (dashed) and DMF (solid). Conditions: 1 mM catalyst with 0.1 M $TBAPF_6$; scan rate: 100 mV/s.

Upon saturation of the electrochemical solution with CO_2, CVs of 4,4'-NH_2-Re display a moderate increase in current density with an onset more positive than the first reduction event under N_2 (Figures 4 and S7). The maximum current density reaches nearly 2 mA/cm^2, greater than the maximum current densities of both 5,5'-NH_2-Re and 6,6'-NH_2-Re (each <1 mA/cm^2). Various Brønsted acids, such as water, 2,2,2-trifluoroethanol (TFE), and phenol, were evaluated as proton sources for the reduction of CO_2 for both 4,4'-NH_2-Re and 5,5'-NH_2-Re (Figures 4 and S8-S10). With the addition of 1 M acid, 4,4'-NH_2-Re displayed a trend similar to that observed for 6,6'-NH_2-Re, with TFE providing the greatest current density of 9.3 mA/cm^2 at -2.40 V. While this current enhancement is observed at a potential >200 mV more negative than that at which 6,6'-NH_2-Re achieved the maximum current density (-2.13 V), the current increase is approximately three times greater (Figure 5a). The complex 5,5'-NH_2-Re, however, reached the greatest current density of 6.2 mA/cm^2 with 1 M PhOH, at the same potential as the one observed for 4,4'-NH_2-Re (-2.40 V) (Figures 5b and S11-S13). Addition of water to both complexes leads to a negligible increase in current. For consistency, TFE was used for all further electrochemical studies. Since PhOH is poorly behaved under N_2 (see additional discussion below), TFE was selected to minimize the possibility of competing side reactions, such as proton reduction.

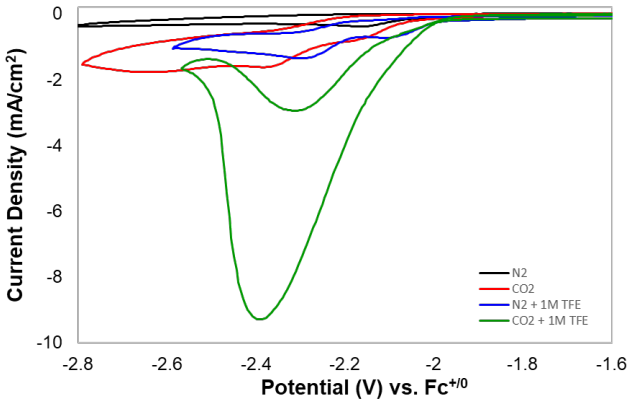

Figure 4. CVs of 4,4'-NH_2-Re under N_2 (black), CO_2 (red), N_2 + 1 M TFE (blue), and CO_2 + 1 M TFE (green). Conditions: 1 mM catalyst in MeCN with 0.1 M $TBAPF_6$; scan rate: 100 mV/s.

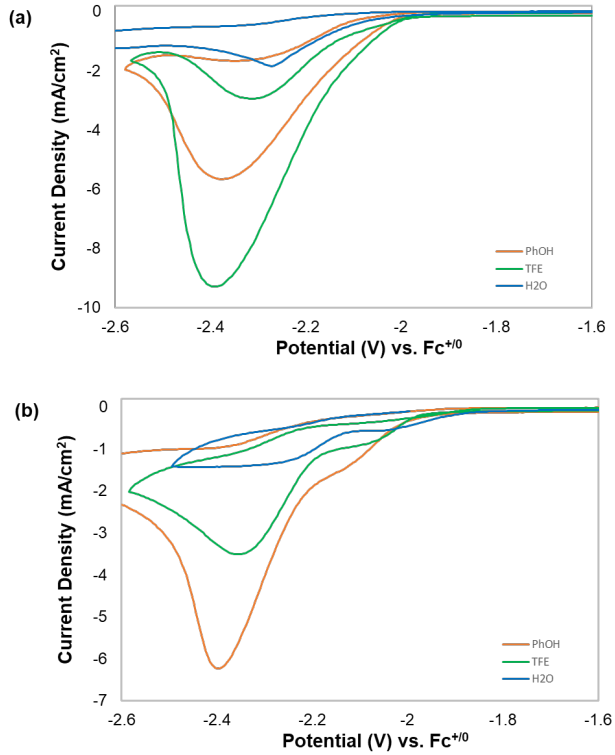

Figure 5. CVs of 1 mM (a) 4,4'-NH_2-Re and (b) 5,5'-NH_2-Re under CO_2 with 1 M PhOH (orange), 1 M TFE (green), and 1 M H_2O (blue). Conditions: 1 mM catalyst in MeCN with 0.1 M $TBAPF_6$; scan rate: 100 mV/s.

Interestingly, 4,4'-NH_2-Re and 5,5'-NH_2-Re have catalytic onset potentials and maximum current density potentials that are more negative than those of 6,6'-NH_2-Re (Figure 6). This suggests that the position of the NH_2 group likely plays an important role in the catalytic mechanism. As has been observed for other CO_2 reduction catalysts, available pendant proton donors in close proximity to the metal center can help stabilize the CO_2 adduct that forms during catalysis, allowing the reduction of CO_2 to occur with a lower overpotential. In the NH_2-substituted catalysts, this trend is only observed with addition of Brønsted acids and is not seen under CO_2 alone, indicating that the acid source itself may participate in hydrogen bonding interactions that influence catalysis, similar to our previous observations and calculations for a

cobalt macrocycle CO_2 reduction catalyst.[14,15] The NH_2 moieties in 4,4'-NH_2-Re and 5,5'-NH_2-Re are likely positioned too far from the rhenium metal center to have a significant effect on the catalytic potentials.

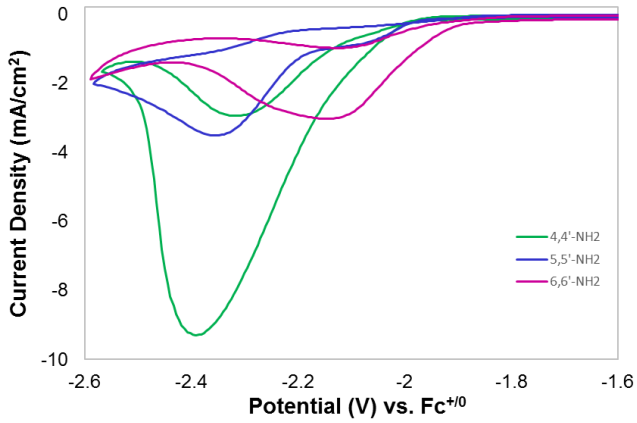

Figure 6. CVs of 4,4'-NH_2-Re (green), 5,5'-NH_2-Re (purple), and 6,6'-NH_2-Re (pink) under CO_2 with 1 M TFE. Conditions: 1 mM catalyst in MeCN with 0.1 M $TBAPF_6$; scan rate 100 mV/s.

Addition of Brønsted acids under N_2 was also performed for both 4,4'-NH_2-Re and 5,5'-NH_2-Re (Figures 7 and S14-S16). While water provides no current increase for 4,4'-NH_2-Re under N_2, addition of 1 M TFE does lead to a slight increase in current density. Addition of 1 M PhOH leads to a significant increase in current density, reaching approximately 4 mA/cm^2, which is not substantially lower than the current density achieved under CO_2 (5.7 mA/cm^2). Without the presence of CO_2 for catalytic CO production, these results imply that some other process, such as proton reduction, may be occurring due to the presence of the added proton source. PhOH has a smaller pK_a in MeCN than TFE and water, making it a stronger proton donor relative to the other two. This acidity difference likely explains why the increase in current density is more substantial with the addition of PhOH compared to the other Brønsted acids.[38] Interestingly, 5,5'-NH_2-Re displays a similar increase in current density with the addition of PhOH, reaching >7 mA/cm^2, which is slightly greater than the current density with 1 M PhOH under CO_2. Since the maximum current density for 5,5'-NH_2-Re under N_2 occurs at a potential more negative than that under CO_2, this process may not compete with CO_2 reduction at less negative potentials.

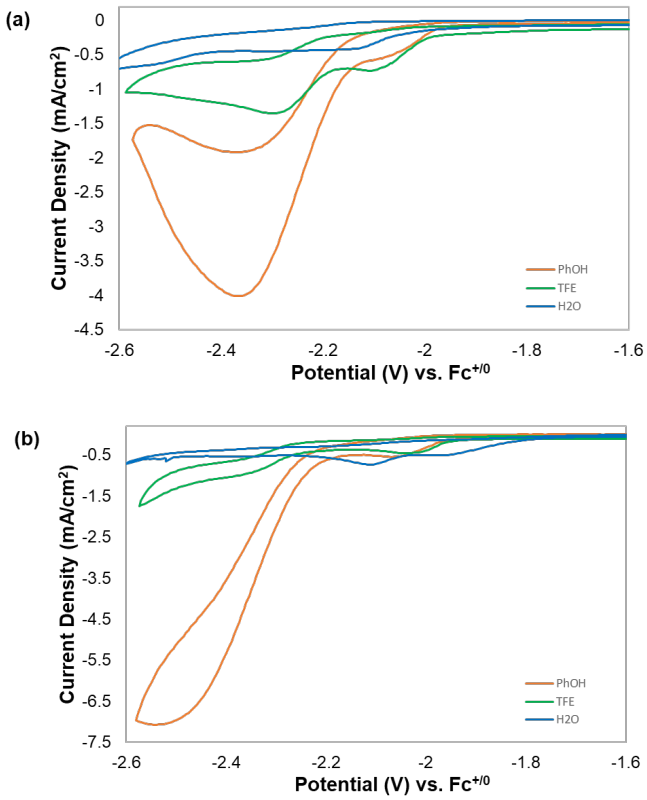

Figure 7. CVs of 1 mM (a) 4,4'-NH_2-Re and (b) 5,5'-NH_2-Re under N_2 with 1 M PhOH (orange), 1 M TFE (green), and 1 M H_2O (blue). Conditions: 1 mM catalyst in MeCN with 0.1 M $TBAPF_6$; scan rate: 100 mV/s.

3.3. Controlled Potential Electrolysis

Controlled potential electrolysis (CPE) studies of 4,4'-NH_2-Re were performed for one hour under CO_2 with added TFE (1 M) at various electrochemical potentials (Figure 8). Gas chromatography (GC) was used for analysis of the headspace of the CPE cell after electrolysis (Figure S26). All CPE results for 4,4'-NH_2-Re are presented in Table 2. Current versus time plots display a decrease in current over time at each potential, indicating long-term instability of this catalyst. The highest catalytic activity (FE_{CO} = 91%, 65 µmol CO) is observed at -2.40 V, near the potential of maximum current density observed in the CV studies with added TFE. At each potential, only CO was produced, with no other products, such as H_2 or formate, observed by GC or ^{1}H NMR analysis. Under N_2, CPE of 4,4'-NH_2-Re at -2.4 V with 1 M TFE yielded a FE_{H2} of 13% and no observable CO production or catalyst degradation.

Similar to the CPE behavior observed for 6,6'-NH_2-Re, 4,4'-NH_2-Re displays a dependence of FE_{CO} on electrochemical potential, with greater amounts of CO produced and higher FE values at more negative potentials. Since this trend is only observed for the NH_2-substituted rhenium bipyridine catalysts, it indicates that the availability of pendant protons does play a role in the catalytic activity, potentially as a proton shuttle for the Brønsted acid. Additionally, the total amounts of CO produced by 4,4'-NH_2-Re are approximately two-fold lower than those produced by 6,6'-NH_2-Re, with lower overall TON, substantiating the beneficial positioning of the pendant amine near the rhenium metal center in 6,6'-NH_2-Re (Table S3).

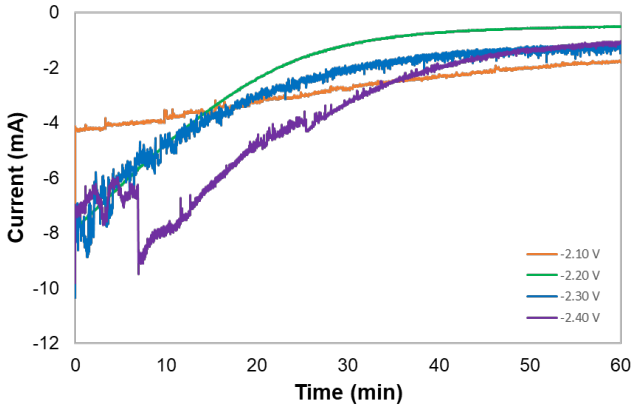

Figure 8. Current versus time over one hour of controlled potential electrolysis of 4,4'-NH_2-Re at -2.10 V (orange), -2.20 V (green), -2.30 V (blue), and -2.40 V (purple). CPE studies were performed using 1 mM catalyst in MeCN with 1 M TFE and 0.1 M $TBAPF_6$.

Table 2. CPE results of 4,4'-NH_2-Re in MeCN under CO_2 with 1 M TFE.

Potential (V)	FE_{CO} (%)	FE_{H2} (%)	µmol CO	TON
-2.10	27	0	14	0.4
-2.20	45	0	19	0.5
-2.30	61	0	32	0.8
-2.40	91	0	65	1.6

Post-catalytic scanning electron microscopy (SEM) and X-ray photoelectron spectroscopy (XPS) were performed on the glassy carbon working electrode to investigate the deactivation observed during CPE of 4,4'-NH_2-Re. CPE was performed for one hour with standard conditions at -2.4 V, and the electrode was collected after catalysis. Three different sections of the electrode were examined – bare (not immersed in the catalytic solution during electrolysis), non-washed (no further modification post-electrolysis), and washed (washed with acetone post-CPE) (Figure S18). Full XPS survey, Re 4f, and Cl 2p spectra as well as various SEM magnifications of all three electrode sections are presented in the SI (Figures S19-S25). In addition to particles shown on the post-catalytic SEM images, XPS spectra clearly show the presence of Re on the electrode, indicating deposition of Re nanoparticles or catalyst molecules. This loss of Re from the active catalyst is a likely explanation for the decrease in current over time.

3.4 Computational Studies

A series of unrestricted density functional theory (DFT) calculations were performed on 4,4'-NH_2-Re, 5,5'-NH_2-Re, and 6,6'-NH_2-Re to probe the electronic implication of amine position on the bipyridine ligand (Tables S4-S6). Optimized structures of these complexes are in good agreement with the structures obtained through X-ray crystallographic techniques (Table S2). Based on these calculations, HOMOs of both 4,4'-NH_2-Re and 6,6'-NH_2-Re display significant stabilization compared to the HOMO of 5,5'-NH_2-Re (by 11 and 35 eVs, respectively) (Figure 9). Moreover, both 4,4'-NH_2-Re and 6,6'-NH_2-Re exhibit significantly more HOMO orbital contribution from both the metal center and equatorial CO ligands compared to the HOMOs of 5,5'-NH_2-Re, while the HOMO of 4,4'-NH_2-Re exhibits the lowest contribution from the bipyridine ligand (Figure 9). Upon comparing the HOMO-LUMO gap of these complexes, the following trend of 4,4'-NH_2-Re > 6,6'-NH_2-Re > 5,5'-NH_2-Re was determined. To evaluate if electron density

on the metal center is dependent on amine positionality, Mulliken electron population analysis was performed on each NH_2-Re complex. Based on these calculations, the metal center of 6,6'-NH_2-Re (+0.748) displays the lowest partial positive charge compared to 5,5'-NH_2-Re (+0.830) and 4,4'-NH_2-Re (+0.834), indicating a greater degree of electron density on the metal center for 6,6'-NH_2-Re compared to its related congeners. In addition to hydrogen bonding interactions, this trend supports the more positive reduction potential of 6,6'-NH_2-Re than those of the 4,4'- and 5,5'- analogues, which are very similar, substantiating that both sterics and electronics play a role in the catalytic activity.

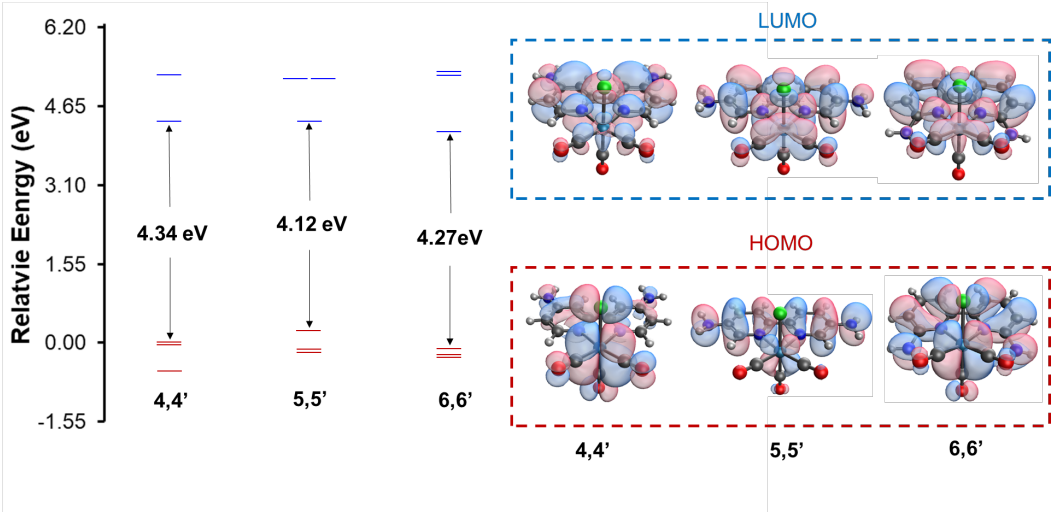

Figure 9. Molecular orbital scheme of complexes 4,4'-NH_2-Re, 5,5'-NH_2-Re, 6,6'-NH_2-Re (left), with the corresponding orbital images of HOMO and LUMO (right). Calculations were performed using the M06 functional with the 6-311G* basis set for H, C, N, and O atoms and the LANL2DZ effective core potential and basis set for Cl and Re atoms.

4. Conclusions

In summary, a novel 4,4'-NH_2 substituted rhenium bipyridine catalyst, 4,4'-NH_2-Re, was synthesized and characterized, and its electrochemical behavior was investigated and compared to that of the previously studied 5,5'- and 6,6'-analogues. Electrochemistry under both N_2 and CO_2 display key differences between 4,4'-NH_2-Re and 6,6'-NH_2-Re, indicating that the position of the primary amine on the bipyridine backbone influences the formation of hydrogen bonding interactions and electron density of the metal center. Additionally, catalytic studies demonstrate a more negative onset potential and catalytic overpotential for 4,4'-NH_2-Re and 5,5'-NH_2-Re compared to 6,6'-NH_2-Re. Although 4,4'-NH_2-Re shows a similar trend to 6,6'-NH_2-Re of FE_{CO} dependence on electrochemical potential, the lower overall production of CO and more negative optimized catalytic potential indicate that positioning of the primary amine farther from the metal center negatively impacts electrocatalytic activity. The observed trends are supported by DFT studies, which further indicate that the greater electron density on the Re center for 6,6'-NH_2-Re is more favorable for CO_2 reduction.

CRediT authorship contribution statement

Ashley N. Hellman: Methodology, Formal analysis, Investigation, Writing – original draft.
Jeremy A. Intrator: performed DFT studies, analysis, and writing.
Jeremiah Choate: recrystallization and electrolysis studies, analysis, and writing.

David A. Velazquez: X-ray crystallography studies, analysis, and writing.
Smaranda C. Marinescu: Conceptualization, Resources, Writing – review & editing, Supervision, Project administration.

Declaration of Competing Interest

The authors declare that they have no known competing financial interests or personal relationships that could have appeared to influence the work reported in this paper.

Supplementary Data

The supplementary crystallographic data for 4,4'-NH_2-Re was deposited on the CCDC website, under CCDC number of 2167226.

Acknowledgements

This work was supported by the National Science Foundation (NSF) through the awards CHE-1555387 and CHE-2102707, and by the University of Southern California (USC). We are grateful to the USC Wrigley Institute for the Norma and Jerol Sonosky summer fellowship to ANH. NMR, FTIR and UV-vis, X-ray, XPS, and SEM data were collected with instrumentation provided by USC. We would like to thank the National Science Foundation (award: CHE-2018740) for the purchase of the Rigaku diffractometer used to solve the crystal structure reported here.

References

[1] D. G. Nocera, *Acc. Chem. Res.* **2017**, *50*, 616–619.

[2] P. De Luna, C. Hahn, D. Higgins, S. A. Jaffer, T. F. Jaramillo, E. H. Sargent, *Science.* **2019**, *364*, 350.

[3] E. E. Benson, C. P. Kubiak, A. J. Sathrum, J. M. Smieja, *Chem. Soc. Rev.* **2009**, *38*, 89–99.

[4] W. Lubitz, H. Ogata, O. Rü, E. Reijerse, *Chem. Rev.* **2014**, *114*, 4081–4148.

[5] H. Dobbek, V. Svetlitchnyi, L. Gremer, R. Huber, O. Meyer, *Science.* **2001**, *293*, 1281–1285.

[6] J.-H. Jeoung, H. Dobbek, *Science.* **2007**, *318*, 1461–1464.

[7] A. W. Nichols, C. W. Machan, *Front. Chem.* **2019**, *7*, 397.

[8] E. Fujita, C. Creutz, N. Sutin, B. S. Brunschwig, *J. Am. Chem. Soc* **1993**, *32*, 2657–2662.

[9] J. Schneider, H. Jia, K. Kobiro, D. E. Cabelli, J. T. Muckerman, E. Fujita, *Energy Environ. Sci.* **2012**, *5*, 9502–9510.

[10] J. D. Froehlich, C. P. Kubiak, *Inorg. Chem* **2012**, *51*, 3932–3934.

[11] C. Costentin, G. Passard, M. Robert, J.-M. Savéant, *Proc. Natl. Acad. Sci.* **2014**, *111*, 14990–14994.

[12] I. Azcarate, C. Costentin, M. Robert, J.-M. Saveánt, *J. Am. Chem. Soc.* **2016**, *138*, 16639–16644.

[13] J. W. Jurss, R. S. Khnayzer, J. A. Panetier, K. A. El Roz, E. M. Nichols, M. Head-Gordon, J. R. Long, F. N. Castellano, C. J. Chang, *Chem. Sci.* **2015**, *6*, 4954–4972.

[14] A. Chapovetsky, T. H. Do, R. Haiges, M. K. Takase, S. C. Marinescu, *J. Am. Chem. Soc.* **2016**, *138*, 5765–5768.

[15] A. Chapovetsky, M. Welborn, J. M. Luna, R. Haiges, T. F. Miller III, S. C. Marinescu, *ACS Cent. Sci.* **2018**, *4*, 397–404.

[16] A. Chapovetsky, J. J. Liu, M. Welborn, J. M. Luna, T. Do, R. Haiges, T. F. Miller, S. C. Marinescu, *Inorg. Chem.* **2020**, *59*, 13709–13718.

[17] S. Sung, D. Kumar, M. Gil-Sepulcre, M. Nippe, *J. Am. Chem. Soc* **2017**, *139*, 13993–13996.

[18] L. Rotundo, C. Garino, E. Priola, D. Sassone, H. Rao, B. Ma, M. Robert, J. Fiedler, R. Gobetto, C. Nervi, *Organometallics* **2019**, *38*, 1351–1360.

[19] S. A. Chabolla, C. W. Machan, J. Yin, E. A. Dellamary, S. Sahu, N. C. Gianneschi, M. K. Gilson, F. A. Tezcan, C. P. Kubiak, *Faraday Discuss.* **2017**, *198*, 279–300.

[20] S. S. Saund, M. A. Siegler, V. S. Thoi, **2021**, *18*, 54.

[21] N. S. Idris, J. M. Barlow, S. A. Chabolla, J. W. Ziller, J. Y. Yang, *Polyhedron* **2021**, *208*, 115385.

[22] G. F. Manbeck, J. T. Muckerman, D. J. Szalda, Y. Himeda, E. Fujita, *J. Phys. Chem. B* **2015**, *119*, 7457–7466.

[23] J. O. Taylor, G. Neri, L. Banerji, A. J. Cowan, F. Hartl, *Inorg. Chem.* **2020**, *59*, 5564–5578.

[24] E. Haviv, D. Azaiza-Dabbah, R. Carmieli, L. Avram, J. M. L. Martin, R. Neumann, *J. Am. Chem. Soc.* **2018**, *140*, 12451–12456.

[25] K. Talukdar, S. S. Roy, E. Amatya, E. A. Sleeper, P. Le Magueres, J. W. Jurss, *Inorg. Chem.* **2020**, *59*, 6087–6099.

[26] C. W. Machan, S. A. Chabolla, J. Yin, M. K. Gilson, F. A. Tezcan, C. P. Kubiak, *J. Am. Chem. Soc.* **2014**, *136*, 14598–14607.

[27] C. W. Machan, J. Yin, S. A. Chabolla, M. K. Gilson, C. P. Kubiak, *J. Am. Chem. Soc.* **2016**, *138*, 8184–8193.

[28] D. A. Popov, J. M. Luna, N. M. Orchanian, R. Haiges, C. A. Downes, S. C. Marinescu, *Dalt. Trans.* **2018**, *47*, 17450–17460.

[29] A. N. Hellman, R. Haiges, S. C. Marinescu, *Dalt. Trans.* **2019**, *48*, 14251–14255.

[30] M. H. Rønne, D. Cho, M. R. Madsen, J. B. Jakobsen, S. Eom, É. Escoudé, H. C. D. Hammershøj, D. U. Nielsen, S. U. Pedersen, M. H. Baik, T. Skrydstrup, K. Daasbjerg, *J. Am. Chem. Soc.* **2020**, *142*, 4265–4275.

[31] J. Agarwal, T. W. Shaw, H. F. Schaefer, A. B. Bocarsly, *Inorg. Chem.* **2015**, *54*, 5285–5294.

[32] F. Franco, C. Cometto, F. F. Vallana, F. Sordello, E. Priola, C. Minero, C. Nervi, R. Gobetto, *Chem. Commun.* **2014**, *50*, 14670–14673.

[33] K. T. Ngo, M. McKinnon, B. Mahanti, R. Narayanan, D. C. Grills, M. Z. Ertem, J. Rochford, *J. Am. Chem. Soc.* **2017**, *139*, 2604–2618.

[34] S. Sung, X. Li, L. M. Wolf, J. R. Meeder, N. S. Bhuvanesh, K. A. Grice, J. A. Panetier, M. Nippe, *J. Am. Chem. Soc* **2019**, *141*, 6569–6582.

[35] S. S. Roy, K. Talukdar, J. W. Jurss, *ChemSusChem* **2021**, *14*, 662–670.

[36] J. Mukherjee, I. Siewert, *Eur. J. Inorg. Chem.* **2020**, *2020*, 4319–4333.

[37] S. A. Chabolla, E. A. Dellamary, C. W. Machan, F. A. Tezcan, C. P. Kubiak, *Inorganica Chim. Acta* **2014**, *422*, 109–113.

[38] M. L. Clark, L. Cheung, M. Lessio, E. A. Carter, C. P. Kubiak, *ACS Catal.* **2018**, *8*, 2021–2029.

[39] S. E. Tignor, H. Y. Kuo, T. S. Lee, G. D. Scholes, A. B. Bocarsly, *Organometallics* **2019**, *38*, 1292–1299.

[40] L. Rotundo, E. Azzi, A. Deagostino, C. Garino, L. Nencini, E. Priola, P. Quagliotto, R. Rocca, R. Gobetto, C. Nervi, *Front. Chem.* **2019**, *7*, 417.

[41] R. Bikas, E. Shahmoradi, N. Noshiranzadeh, M. Emami, S. Reinoso, *Inorganica Chim. Acta* **2017**, *466*, 100–109.

[42] R. Bikas, V. Lippolis, N. Noshiranzadeh, H. Farzaneh-Bonab, A. J. Blake, M. Siczek, H. Hosseini-Monfared, T. Lis, *Eur. J. Inorg. Chem.* **2017**, *2017*, 999–1006.

[43] A. N. Hellman, R. Haiges, S. C. Marinescu, *ChemElectroChem* **2021**, *8*, 1864–1872.

[44] Y. Shao, L. F. Molnar, Y. Jung, J. Kussmann, C. Ochsenfeld, S. T. Brown, A. T. B. Gilbert, L. V.

Slipchenko, S. V. Levchenko, D. P. O'Neill, R. A. DiStasio Jr, R. C. Lochan, T. Wang, G. J. O. Beran, N. A. Besley, J. M. Herbert, C. Yeh Lin, T. Van Voorhis, S. Hung Chien, A. Sodt, R. P. Steele, V. A. Rassolov, P. E. Maslen, P. P. Korambath, R. D. Adamson, B. Austin, J. Baker, E. F. C. Byrd, H. Dachsel, R. J. Doerksen, A. Dreuw, B. D. Dunietz, A. D. Dutoi, T. R. Furlani, S. R. Gwaltney, A. Heyden, S. Hirata, C.-P. Hsu, G. Kedziora, R. Z. Khalliulin, P. Klunzinger, A. M. Lee, M. S. Lee, W. Liang, I. Lotan, N. Nair, B. Peters, E. I. Proynov, P. A. Pieniazek, Y. Min Rhee, J. Ritchie, E. Rosta, C. David Sherrill, A. C. Simmonett, J. E. Subotnik, H. Lee Woodcock III, W. Zhang, A. T. Bell, A. K. Chakraborty, D. M. Chipman, F. J. Keil, A. Warshel, W. J. Hehre, H. F. Schaefer III, J. Kong, A. I. Krylov, P. M. W. Gill, M. Head-Gordon, *Phys. Chem. Chem. Phys.* **2006**, *8*, 3172–3191.

[45] R. Ditchfield, W. J. Hehre, J. A. Pople, *J. Chem. Phys.* **1971**, *54*, 724–728.

[46] W. J. Hehre, R. Ditchfield, J. A. Pople, *J. Chem. Phys.* **1972**, *56*, 2257–2261.

[47] P. C. Hariharan, J. A. Pople, *Theor. Chim. Acta* **1973**, *28*, 213–222.

[48] D. Feller, *J. Comput. Chem.* **1996**, *17*, 1571–1586.

[49] K. L. Schuchardt, B. T. Didier, T. Elsethagen, L. Sun, V. Gurumoorthi, J. Chase, J. Li, T. L. Windus, *J. Chem. Inf. Model.* **2007**, *47*, 1045–1052.

[50] P. J. Hay, W. R. Wadt, *J. Chem. Phys.* **1985**, *82*, 270–283.

[51] W. R. Wadt, P. J. Hay, *J. Chem. Phys.* **1985**, *82*, 284–298.

[52] J. Towns, T. Cockerill, M. Dahan, I. Foster, K. Gaither, A. Grimshaw, V. Hazlewood, S. Lathrop, D. Lifka, G. D. Peterson, R. Roskies, J. R. Scott, N. Wilkins-Diehr, *Comput. Sci. Eng.* **2014**, *16*, 62–74.

[53] Y. Zhao, D. G. Truhlar, *Theor. Chem. Acc.* **2008**, *120*, 215–241.

[54] A. Klamt, G. Schüürmann, *J. Chem. Soc. Perkin Trans. 2* **1993**, 799–805.

[55] C. Kremer, G. Schnakenburg, A. Lutzen, *Beilstein J. Org. Chem.* **2014**, *10*, 814–824.

[56] M. Albrecht, I. Janser, A. Lützen, M. Hapke, R. Fröhlich, P. Weis, *Chem. - A Eur. J.* **2005**, *11*, 5742–5748.

[57] B. P. Sullivan, C. M. Bolinger, D. Conrad, W. J. Vining, T. J. Meyer, *J. Chem. Soc. Chem. Commun.* **1985**, 1414–1415.

[58] K. A. Grice, C. P. Kubiak, in *Adv. Inorg. Chem.*, **2014**, pp. 163–188.

[59] A. V. Raghu, G. S. Gadaginamath, M. Priya, P. Seema, H. M. Jeong, T. M. Aminabhavi, *J. Appl. Polym. Sci.* **2008**, *110*, 2315–2320.

[60] A. V. Raghu, H. M. Jeong, *J. Appl. Polym. Sci.* **2008**, *107*, 3401–3407.

TOC Figure:

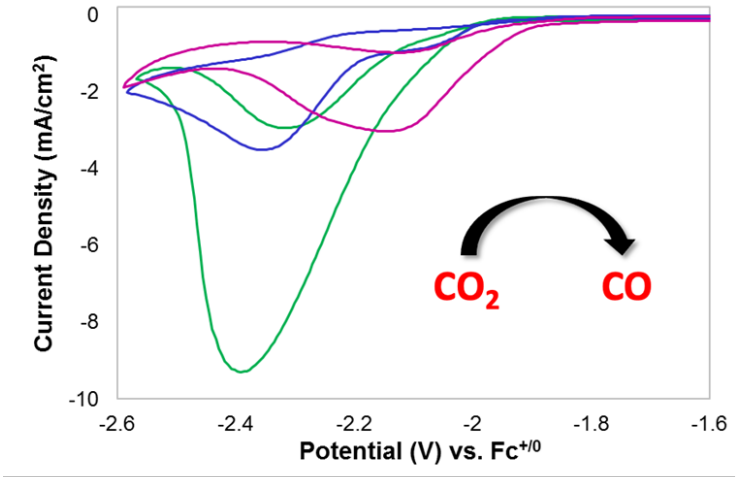

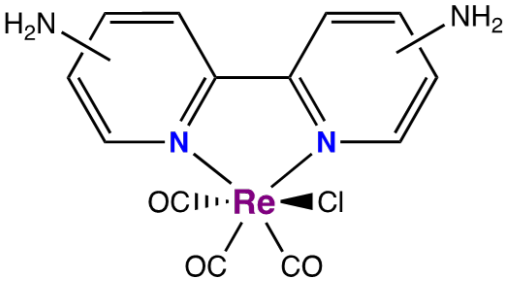

4,4'-NH_2-Re
5,5'-NH_2-Re
6,6'-NH_2-Re